Experimental validation of photoacoustic k-space propagation models

B. T. Cox, J. Laufer, K. Köstli and P. Beard

Department of Medical Physics and Bioengineering, University College London, Shropshire House, 11-20 Capper St., London WC1E 6JA, UK

ABSTRACT

Propagation models to predict the temporal output of a sensor in response to an arbitrary photoacoustically generated initial pressure distribution have been developed. **k**-space (frequency-wavenumber) implementations have been studied with the aim of producing fast and accurate predictions. The **k**-space models have several advantages. They may be implemented using the Fast Fourier transform, which makes them efficient, and the impulse response of the sensor may be straightforwardly included, which makes them more accurate. Also, there is a closely related inverse scheme - a 3D photoacoustic imaging algorithm. Studying the forward problem provides insight into the inverse problem and may indicate ways in which the imaging can be improved. For instance, a validated model of the detector response may be used to improve the spatial resolution of an image reconstructed from measurements via deconvolution. The propagation models were experimentally validated. Broadband (30 MHz) ultrasonic pulses were generated in water by illuminating thin polymer sheets and other optically-absorbent targets with a Q switched Nd:YAG laser (1064 nm, 6 ns pulse duration). The output of the Fabry Perot polymer film sensor was compared to the models' predictions.

Keywords: photoacoustic, propagation model, wavenumber, FFT

1. INTRODUCTION

There are several mechanisms by which electromagnetic radiation incident on a solid or fluid can generate acoustic waves, e.g. ablation, electrostriction or thermoelastic expansion.[1] Photoacoustic imaging is based on the rapid thermoelastic expansion of, predominantly, blood vessels following absorption of a visible or near-infrared laser pulse. The recent demonstration of functional photoacoustic imaging of a rat's brain[2,3] and work on 3D blood vessel and capillary imaging[4,5] have shown that this technique will have many practical biomedical applications. Photoacoustic imaging is an inverse problem. Techniques for numerically solving the equivalent forward problem are useful both for modelling the passage of the sound and for use in matched-field type solutions to imaging and inverse problems.

Many models of ultrasound propagation through tissue were designed with traditional B-mode ultrasound scanning in mind. In this imaging technique it is acoustic inhomogeneities that provide the imaging contrast. Therefore, when modelling sound propagation in these systems, it is necessary to take these acoustic inhomogeneities into account. For this reason, finite element (FE) or finite difference (FD) methods, computer-intensive but very flexible techniques, are widely used for this purpose. However, where tissues may be treated as acoustically homogeneous, as is generally assumed to be the case in photoacoustic imaging, it is quicker to use **k**-space or spectral methods to model the propagation. Through use of the FFT, and because spectral methods require far fewer points per wavelength than FE or FD methods, efficient algorithms may be developed. The two propagation models presented here fall into the category of wavenumber integration algorithms. Propagation models based on numerically solving a wavenumber integral are in widespread use in underwater acoustics and seismology.[6] However, similar techniques have not been applied to the specific problem of the propagation of photoacoustic pulses.

A numerical model of photoacoustic propagation that can include an arbitrary initial pressure distribution has been proposed by Paltauf *et al.* It is based on Poisson's integral solution to the wave equation[7,8] and, while

Send correspondence to B. T. Cox. E-mail: bencox@medphys.ucl.ac.uk

Proc. SPIE **5320**, pp 238-248, 2004
SPIE BIOS 2004, 25-26 January 2004, San Jose, USA

this is an intuitive method and useful for predicting the time evolution of the pressure at a point, to include the averaging effect of a finite-sized detector requires a time-consuming convolution. A **k**-space model which can include small variations in the density has been proposed by Tabei *et al.*[9] This technique calculates the pressure field on a mesh of points. However, as it approximates the time derivatives with finite-differences, the time steps must be small in order for the algorithm to remain stable. In contrast, the first model presented here, while using a similar mesh of points, calculates the pressure field using an exact time-propagator and there is no timestep limitation. Our second model, rather than using the FFT to calculate the pressure everywhere on a mesh in time steps, calculates the pressure on one z-plane for many times at once. For many applications this can result in a significant increase in speed. This model is also useful for calculating single-frequency radiation patterns from photoacoustic sources. The effect of a finite-sized, planar, detector on the measured pressure can be included simply in either model.

2. PROPAGATION MODELS

2.1. Wave Equation

If τ and p represent small temperature and pressure fluctuations in an inviscid fluid they may be related by the coupled linear equations[10]

$$\nabla^2 p = \frac{\gamma}{c^2}\frac{\partial^2}{\partial t^2}(p - \alpha\tau) \tag{1}$$

$$\nabla^2 \tau = \frac{\rho C_p}{K}\frac{\partial}{\partial t}\left(\tau - \frac{\gamma - 1}{\alpha\gamma}p\right) \tag{2}$$

where γ is the ratio of specific heat capacities, c is the sound speed, t is the time, ρ is the density, C_p is the specific heat capacity at constant pressure, K is the thermal conductivity, and $\alpha = \beta\gamma/c^2\rho$, where β is the isobaric volume expansion coefficient. If the thermal conductivity is negligible then $\tau \approx (\gamma - 1)p/\alpha\gamma$ and Eq. (1) reduces to the wave equation

$$\nabla^2 p - \frac{1}{c^2}\frac{\partial^2 p}{\partial t^2} = 0 \tag{3}$$

2.2. Green's Function Solution

A laser pulse incident on a purely absorbing fluid is absorbed and causes a local increase in temperature and pressure. If the pulse is much shorter than the time it would take for sound to travel across the heated region then it may be considered as instantaneous and the distribution of pressure at that instant ($t = 0$) is called the initial pressure distribution $p_0(\mathbf{x})$, for a position $\mathbf{x} = (x, y, z)$. This condition is known as stress-confinement and requires that the laser pulse duration t_p

$$t_p \ll \frac{1}{\mu_a c} \tag{4}$$

where μ_a is the optical absorption coefficient of the medium (and $1/\mu_a$, the optical penetration depth, is a length characteristic of the heated region). With this condition fulfilled, solving Eq. (3) becomes an initial-value problem with $p_0(\mathbf{x})$ as the initial value. By additionally assuming that the particle velocity is initially zero everywhere, the Green's function solution to this initial-value problem in free-space is

$$p(\mathbf{x}, t) = \frac{1}{c^2}\frac{\partial}{\partial t}\int_V p_0(\mathbf{x}')G(\mathbf{x}, t; \mathbf{x}')\,\mathrm{d}\mathbf{x}' \tag{5}$$

where $t \geq 0$ and G is the free space Green's function

$$G(\mathbf{x}, t; \mathbf{x}', t') = \frac{\delta(|\mathbf{x} - \mathbf{x}'| - ct)}{|\mathbf{x} - \mathbf{x}'|} \tag{6}$$

This may be written in the Fourier representation, in terms of the wavevector $\mathbf{k} = (k_x, k_y, k_z)$ and frequency ω, as a fourfold integral[11]

$$G(\mathbf{x}, t; \mathbf{x}') = \frac{1}{(2\pi)^4}\iint \frac{\mathrm{e}^{\mathrm{i}\mathbf{k}.(\mathbf{x}-\mathbf{x}')}\mathrm{e}^{-\mathrm{i}\omega t}}{k^2 - (\omega/c)^2}\,\mathrm{d}\omega\,\mathrm{d}\mathbf{k} \tag{7}$$

where $k = |\mathbf{k}|$.

The two algorithms below for calculating $p(\mathbf{x}, t)$ from the initial pressure $p_0(\mathbf{x})$ are derived by analytically evaluating, in the first case, the ω integral in Eq. (7) and, in the second case, the integral over the vertical wavenumber k_z. The first results in a time-stepping solution for the whole field and the second in a method that calculates the pressure as a function of time at all points on a single z-plane.

2.3. k-Space Model I

The ω integral in Eq. (7) may be rewritten as

$$\int \frac{\mathrm{e}^{\mathrm{i}\mathbf{k}.(\mathbf{x}-\mathbf{x}')}\mathrm{e}^{-\mathrm{i}\omega t}}{(k-\omega/c)(k+\omega/c)}\,\mathrm{d}\omega \tag{8}$$

from which it is clear that there are two simple poles on the real ω axis at $\pm ck$. This can be solved using Cauchy's residue theorem[12] to give

$$G = \frac{c}{(2\pi)^3}\int \frac{\sin(ckt)}{k}\mathrm{e}^{\mathrm{i}\mathbf{k}.(\mathbf{x}-\mathbf{x}')}\,\mathrm{d}\mathbf{k} \tag{9}$$

and hence

$$\frac{\partial G}{\partial t} = \frac{c^2}{(2\pi)^3}\int \cos(ckt)\mathrm{e}^{\mathrm{i}\mathbf{k}.(\mathbf{x}-\mathbf{x}')}\,\mathrm{d}\mathbf{k} \tag{10}$$

Substituting this into Eq. (5) gives a solution for the pressure in a free-field given an initial pressure distribution:

$$p(\mathbf{x}, t) = \frac{1}{(2\pi)^3}\iint p_0(\mathbf{x}')\cos(ckt)\mathrm{e}^{\mathrm{i}\mathbf{k}.(\mathbf{x}-\mathbf{x}')}\,\mathrm{d}\mathbf{k}\,\mathrm{d}\mathbf{x}' \tag{11}$$

Changing the order of the integration gives

$$p(\mathbf{x}, t) = \frac{1}{(2\pi)^3}\int p_0(\mathbf{k})\cos(ckt)\mathrm{e}^{\mathrm{i}\mathbf{k}.\mathbf{x}}\,\mathrm{d}\mathbf{k} \tag{12}$$

where $p_0(\mathbf{k})$ is the 3D spatial Fourier transform of the initial pressure distribution, written, by dropping the primes, as

$$p_0(\mathbf{k}) = \int p_0(\mathbf{x})\mathrm{e}^{-\mathrm{i}\mathbf{k}.\mathbf{x}}\,\mathrm{d}\mathbf{x} \tag{13}$$

This algorithm requires one initial 3D FFT to calculate $p_0(\mathbf{k})$ and then one multiplication and 3D FFT for every subsequent time step. Because the changes of p over time are calculated using the exact propagator $\cos(ckt)$ and not from an approximation it is not necessary to limit the size of time step for stability reasons as in FD methods. The grid spacing must meet the usual criterion to avoid aliasing in the spatial domain; it must be less than half the minimum wavelength. This first **k**-space method is similar to that proposed by Healey *et al.*[13]

2.4. k-Space Model II

In the above section the ω integral in Eq. (7) was calculated analytically. Instead, consider the integral over k_z, the vertical component of the wavevector $\mathbf{k}$. This may be written as

$$\int_{-\infty}^{\infty} \frac{\mathrm{e}^{\mathrm{i}\mathbf{k}.(\mathbf{x}-\mathbf{x}')}\mathrm{e}^{-\mathrm{i}\omega t}}{(k_z-a)(k_z+a)}\,\mathrm{d}k_z \tag{14}$$

where

$$\begin{aligned} a &= \sqrt{(\omega/c)^2 - k_r^2} \qquad &\text{for} \qquad &|\omega/c| > k_r \\ a &= \mathrm{i}\sqrt{k_r^2 - (\omega/c)^2} \qquad &\text{for} \qquad &|\omega/c| < k_r \end{aligned} \tag{15}$$

and $k_r = \sqrt{k_x^2 + k_y^2}$. Eq. (14) may be solved using Cauchy's theorem and, for the case when $|\omega/c| > k_r$, corresponding to propagating waves, the time derivative of the Green's function may be written

$$\frac{\partial G}{\partial t} = \frac{1}{(2\pi)^4} \iiint_{ck_r}^{\infty} \frac{\omega\pi}{a} \mathrm{e}^{\mathrm{i}k_x(x-x')} \mathrm{e}^{\mathrm{i}k_y(y-y')} \left(\mathrm{e}^{-\mathrm{i}a|z'|} \mathrm{e}^{\mathrm{i}\omega t} + \mathrm{e}^{\mathrm{i}a|z'|} \mathrm{e}^{-\mathrm{i}\omega t} \right) \mathrm{d}\omega \, \mathrm{d}k_x \, \mathrm{d}k_y \tag{16}$$

By substituting Eq. (16) into Eq. (5), choosing the measurement plane as $z = z_0$ and assuming $p_0(-z) = p_0(z)$, the following expression for the pressure (contributed by the propagating wavenumber components) may be derived:

$$p(x, y, t; z_0) = \frac{2}{(2\pi)^3 c^2} \iiint_{ck_r}^{\infty} \frac{\omega}{a} \hat{p}_0(k_x, k_y, \omega; z_0) \mathrm{e}^{\mathrm{i}k_x x + \mathrm{i}k_y y} \cos(\omega t) \, \mathrm{d}\omega \, \mathrm{d}k_x \, \mathrm{d}k_y \tag{17}$$

where $a = \sqrt{(\omega/c)^2 - k_x^2 - k_y^2}$. $\hat{p}_0(k_x, k_y, \omega; z_0)$ is interpolated from $\hat{p}_0(\mathbf{k}; z_0)$ using the dispersion relation in Eq. (15) and

$$\hat{p}_0(\mathbf{k}; z_0) = \iiint \left(p_0(x, y, z_0 + z) + p_0(x, y, z_0 - z) \right) \mathrm{e}^{-\mathrm{i}\mathbf{k}.\mathbf{x}} \, \mathrm{d}\mathbf{x} \tag{18}$$

Consider the case where the initial pressure distribution is cylindrically symmetric so that $p_0(\mathbf{x}) = p_0(r, z)$ with no θ dependence. Using $k_r^2 = k_x^2 + k_y^2$, Eqs. (17) and (18) become

$$p(r, t; z_0) = \frac{2}{(2\pi)^3 c^2} \iint_0^{\omega/c} \frac{\hat{p}_0(k_r, \omega; z_0) \omega J_0(k_r r) k_r}{\sqrt{(\omega/c)^2 - k_r^2}} \cos(\omega t) \, \mathrm{d}k_r \, \mathrm{d}\omega \tag{19}$$

where

$$\hat{p}_0(k_r, \omega; z_0) = \iint \left(p_0(r, z_0 + z) + p_0(r, z_0 - z) \right) \mathrm{e}^{-\mathrm{i}z\sqrt{(\omega/c)^2 - k_r^2}} J_0(k_r r) r \, \mathrm{d}z \, \mathrm{d}r \tag{20}$$

The first step in this algorithm is to calculate $\hat{p}_0(k_r, \omega; z_0)$ from the initial pressure $p_0(r, z)$. This need only be done once for each value of z_0 required. The integral over z may be calculated efficiently by performing a FT wrt z and then interpolating via the dispersion relation in Eq. (15) to get p as a function of ω. In the examples given below, the Hankel transform in Eq. (20) wrt r was not calculated directly but $p(r)$ was expressed as $p(x, y)$ and a 2D FFT was used. Numerical integration of the k_r integral in Eq. (19) gives $p(r, \omega; z_0)$, which can be used to generate a single-frequency radiation pattern or, with an additional FFT in ω, the time evolution $p(r, t; z_0)$. When evaluating Eq. (19) numerically it is essential to ensure that the oscillatory parts of the integrand are properly sampled. The singularity at $k_r = \omega/c$ can be removed by making the change of variable $k_r = (\omega/c) \cos\psi$.

To model the *measurement* of the pressure, rather than the pressure at a single point, it is necessary to take into account the averaging effect of a finite-sized detector. A wavenumber model of a planar detector response, D, may be included straightforwardly in either model by multiplying $p_0(\mathbf{k})$ or $\hat{p}_0(k_r, \omega)$ by $D(\mathbf{k})$ or $D(k_r, \omega)$ respectively. For a layered transducer, such as the Fabry-Perot polymer film sensor used here,[14] D can be calculated via a wavenumber approach such as found in Brekhovskikh.[15]

3. EXAMPLES

3.1. Visualisation of the Acoustic Field

Figures 1-4 show examples of pressure fields calculated using model I. Each example shows 8 mm x 8 mm slices through an axis-symmetric 3D pressure field calculated on a 3D mesh of 128^3 points. (z and r both range from -4 to 4 mm.) In Fig. 1 the initial pressure has a tophat profile in r and decays exponentially with $|z|$. In this case, the upper half of p_0 is an image source representing an acoustic reflection from a rigid boundary. An initial pressure distribution such as this, shown in the leftmost image, may be generated in practice by sending a laser pulse along a multimode fibre which terminates in a homogeneous optically absorbing liquid. The other three images are snapshots of the field at 0.6, 1.0 and 1.5 μs later. The negative pressure region that develops close to the fibre-fluid interface - the dark area in the third picture - is due to the edge waves and shows clearly why cavitation has been observed in a case such as this.[16] Figure 2 is similar to Fig. 1

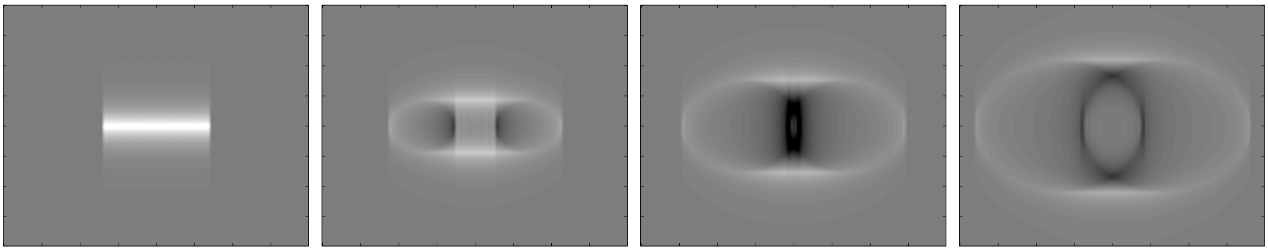

Figure 1. 8 mm x 8 mm slices through the axis-symmetric 3D pressure field with $p_0 = R(r)Z(z)$: $R(r) = 0$ for $r > 1.4$ mm and $R = 1$ otherwise; $Z = \exp(-\mu_a z)$ for +ve z and $Z = V \exp(\mu_a z)$ for −ve z, where $\mu_a = 2.5$ mm^{-1}, is the optical absorption of the fluid and $V = 1$ in this case (rigid boundary). Left to right: initial pressure distribution $p_0(\mathbf{x})$, the pressure $p(\mathbf{x})$ after 0.6 μs, after 1.0 μs, and after 1.5 μs.

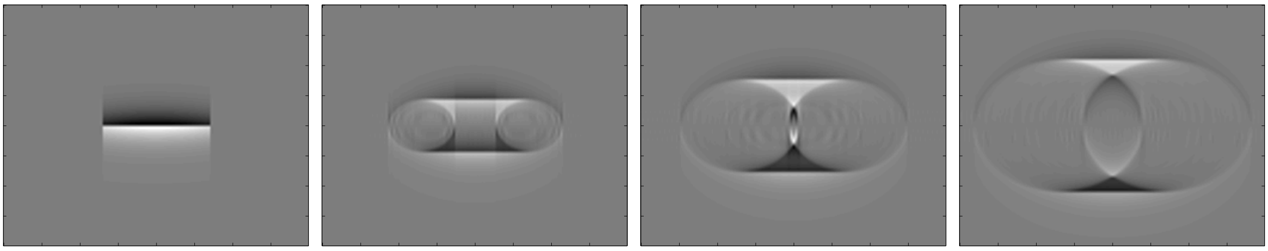

Figure 2. As Fig.1 except $V = -1$. Tophat laser pulse incident on an absorbing fluid at a pressure-release boundary.

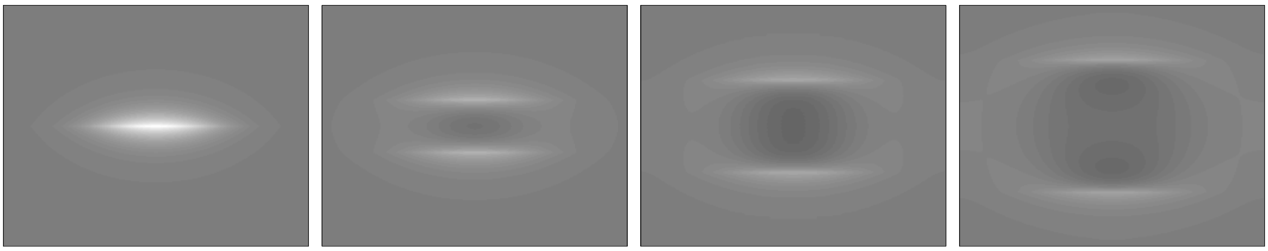

Figure 3. As Fig.1 except $R(r)$ has a Gaussian rather than a tophat profile (1/e point at $r = 2$ mm). Edge waves are not generated.

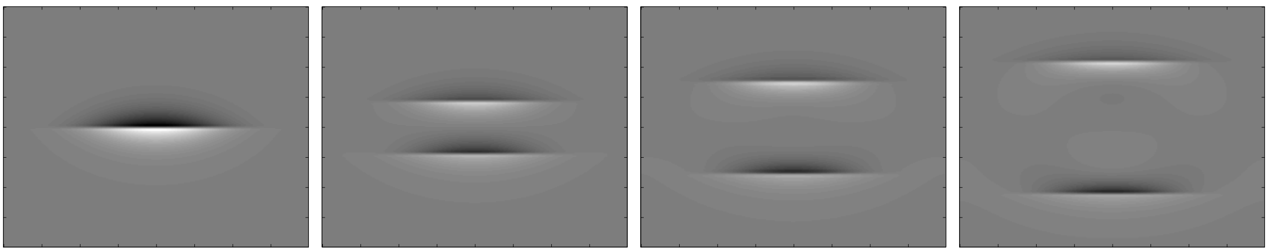

Figure 4. As Fig.2 except $R(r)$ has a Gaussian rather than a tophat profile (1/e point at $r = 2$ mm).

except that instead of modelling a solid-fluid interface at $z = 0$ there is an acoustic pressure-release, air-fluid, boundary. The reflection from this is represented by the negative image in the top half of the leftmost image. This results in a bipolar signal, as the subsequent images show. Figures 3 and 4, in which the tophat profile is replaced with a Gaussian, shows that by removing the sharp radial discontinuity, the edge waves are no longer generated. The signal is bipolar in both cases, but the negative peak is greater in Fig. 3 due to the pressure release boundary.

3.2. Single-Frequency Radiation Patterns

Model II, as well as calculating time responses $p(r, z_0, t)$, can be used to generate single-frequency radiation patterns $p(r, z_0, \omega)$ for photoacoustic sources by calculating just the k_r integral in Eq. (19). Figure 5 shows radiation patterns, in dB, at 2 MHz and 500 kHz for a tophat profile pulse absorbed at a solid-fluid boundary, such as used in Fig. 1. Figure 6 shows radiation patterns for a Gaussian profile pulse absorbed at an air-fluid boundary, such as used in Fig. 3. Note that because this boundary is pressure-release the pressure there is always zero. Clearly the pressure distribution with a Gaussian profile has a more directional radiation pattern.

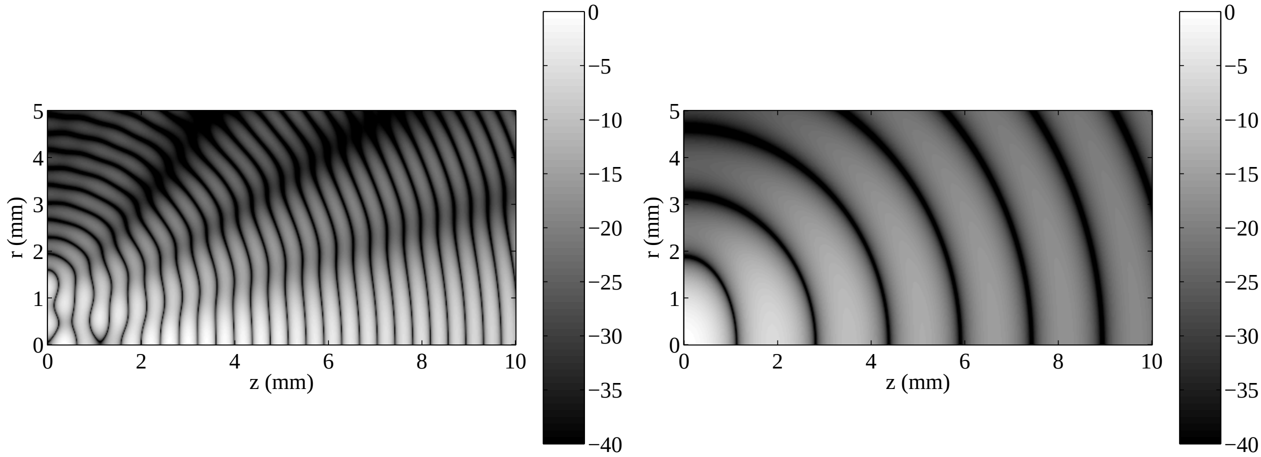

Figure 5. Radiation patterns at 2MHz and 500 kHz, in dB, for a tophat initial pressure distribution at a solid-fluid boundary such as used in Fig. 1. Tophat radius 1.5 mm, $\mu_a = 3$ mm^{-1}, $V = 1$.

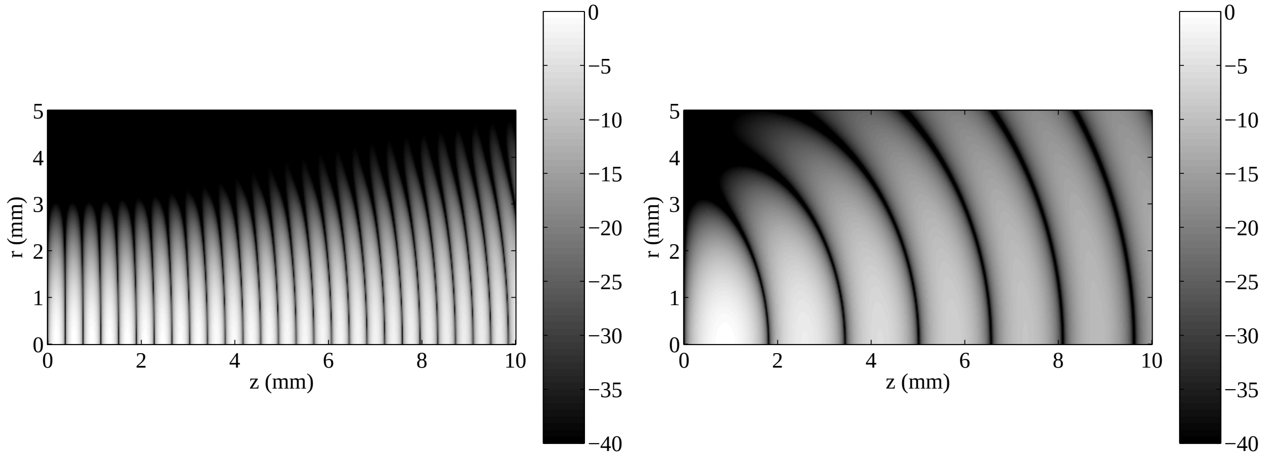

Figure 6. Radiation patterns at 2MHz and 500 kHz, in dB, for a Gaussian initial pressure distribution at an air-fluid boundary such as used in Fig. 3. 1/e point at $r = 1.5$ mm, $\mu_a = 3$ mm^{-1}, $V = -1$.

3.3. Pressure Time Series

Either model I or II may be used to predict the time evolution of the pressure at a point, or at a receiver, due to an initial distribution $p_0(\mathbf{x})$. However, for signals containing high frequencies the mesh required for model I is large and the calculations therefore slow. Model II was, therefore, used to calculate the examples shown below. Figures 7 and 8, except the right-hand graph in Fig. 8, assume a point detector. The left graph in Fig. 7 shows how the pressure at a point on-axis and 10 mm below the surface of a dye changes with time when the initial pressure distribution is radially Gaussian and decreasing exponentially with depth, $\mu_a = 1$ mm^{-1}. The solid line gives the pressure in the case where the boundary is pressure-release (see Fig. 9). The dotted line shows the pressure under the same conditions, except that the boundary is solid (Fig. 10). The righthand

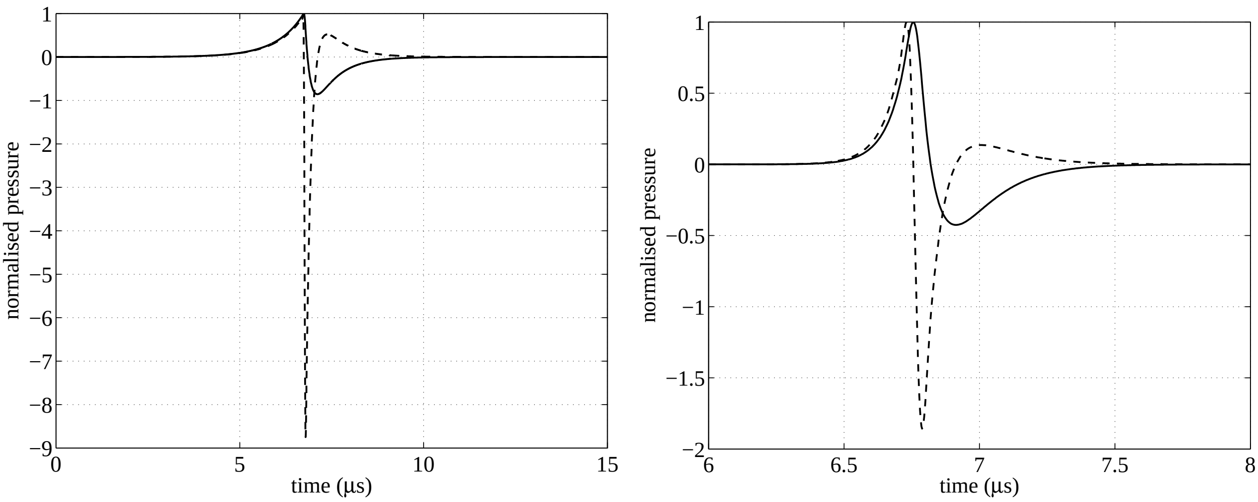

Figure 7. Left: Gaussian radial distribution 1/e point at $r = 2$ mm, $\mu_a = 1$ mm^{-1}, sensor at $r = 0$ mm, $z_0 = 10$ mm, solid line for $V = 1$, dashed line for $V = -1$. Right: as left but with $\mu_a = 10$ mm^{-1}.

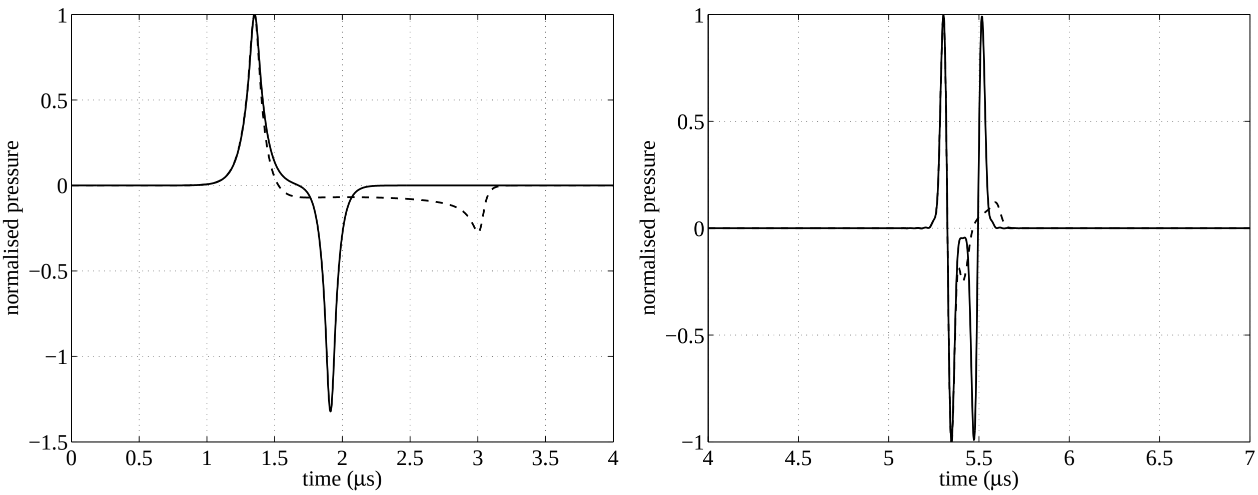

Figure 8. Left: tophat distribution radius 2 mm, $\mu_a = 10$ mm^{-1}, $V = 1$, $z_0 = 2$ mm, solid line for on-axis $r = 0$ mm, dashed line for off-axis $r = 2$ mm. Right: tophat distribution radius 2 mm, $\mu_a = 10$ mm^{-1}, $V = -1$, sensor at $r = 0$ mm, $z_0 = 7.9$ mm, solid line for model not including detector response function D, dashed line for model including detector response $D(k_r) = \sigma^2 J_1(k_r\sigma)/k_r\sigma$ where σ is radius of the sensitive area of the detector.

graph shows the same, except that the optical absorption of the dye is increased to $\mu_a = 10$ mm^{-1}. The initial pressure distribution assumed for the lefthand graph in Fig. 8 had a tophat profile with $\mu_a = 10$ mm^{-1} and a solid boundary above the dye (Fig. 11). The solid line shows the pressure on-axis 2 mm below the dye surface and the dashed line shows the pressure at the same depth but 2 mm off-axis. The righthand graph shows the effect of the spatial averaging inherent in any actual detector. With an initial tophat distribution at a pressure release boundary (radius 2mm, $\mu_a = 10$ mm^{-1}), the solid line shows the pressure at $r = 0$, $z_0 = 7.9$ mm, with a point detector. The dashed line shows the pressure that would be measured at that point by a finite-sized circular detector by including a simple model of the detector in the model. In this case we used a detector response function of the form $D(k_r) = \sigma^2 J_1(k_r\sigma)/k_r\sigma$ where σ is the radius of the sensitive area of the detector[17]; this is equivalent to spatially averaging over a circle of radius σ. As this example shows, it is very important to be able to include the detector response in the model as it can significantly affect the measured pressure signal.

4. EXPERIMENTAL MEASUREMENTS

The output of a Q-switched Nd:YAG laser (1064 nm wavelength, 26 mJ, 6 ns pulse) was directed at optically-absorbing dye or india ink overlying a Fabry-Perot sensor.[14] This sensor consisted of a polymer film coated to produce a low finesse Fabry-Perot interferometer and illuminated by a collimated 850 nm diode laser beam. A pressure wave incident on the sensor caused a change in the optical thickness and could be detected by a change in the intensity of the reflected light. The active detector area is defined by the geometry and profile of the region of the sensor that is optically addressed. The sensor had an effective circular detection area of $\sigma = 0.6$ mm radius and a thickness of 125 μm, giving a frequency response up to $\sim$ 12 MHz. A sensor directivity function $D = \sigma^2 J_1(k_r\sigma)/k_r\sigma$ was included in the model to account for the spatial averaging over the detection area and the model was bandlimited to reflect the limited frequency response. Several experiments were conducted, the details of which are shown in Figs. 9-11. A measurement from each experiment was compared to the output of model II. The stress confinement criterion given in Eq. (4), which must hold for the model to be accurate, requires that optical absorption coefficients $\mu_a \ll 1/t_p c \approx 110$ mm^{-1}, as $c = 1480$ m/s and $t_p \approx 6$ ns. In all these experiments the depth of the dye was measured from the time of arrival of the acoustic signal and subsequently entered into the model. In those cases that used india ink, μ_a was unknown and a value was

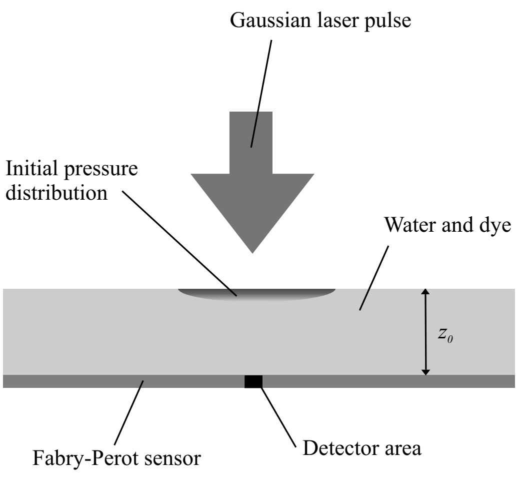

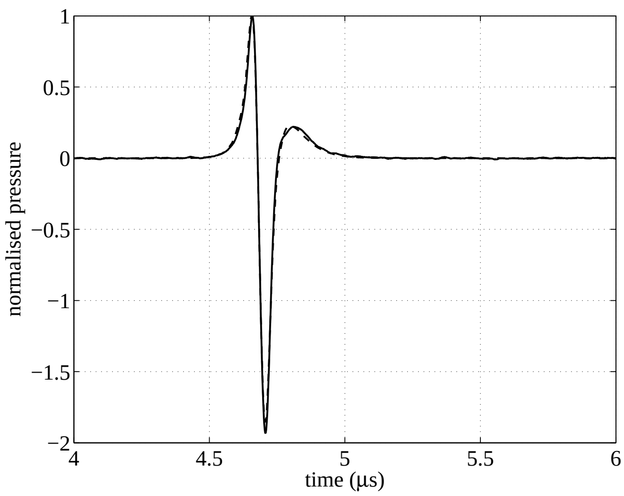

Figure 9. A Gaussian profile laser pulse, $r = 1$ mm at the 1/e point, was directed onto the surface of an optically absorbing india ink solution, $\mu_a = 21.5$ mm^{-1}. The depth of the dye was $z_0 = 6.9$ mm. The Fabry-Perot sensor had a circular sensitive area of effective radius 0.6 mm centred on-axis ($r = 0$), and had a 125 μm thick sensing layer giving a frequency response up to $\sim$ 12 MHz. Solid line: measurement, dashed line: model.

chosen to obtain a match to the measurements. The optical absorption of the water-dye mixtures used was measured independently using an optical transmission technique.

The first experiment used a laser pulse with an approximately Gaussian profile where the laser intensity had dropped to 1/e of its maximum value 1.2 mm from the centre of the beam. The pulse was directed onto the surface of an optically absorbing water-dye mixture, with optical absorption coefficient $\mu_a = 22.5$ mm^{-1}. The surface was exposed to the air. The depth of the dye was $z_0 = 6.9$ mm, i.e. the sensor was this far below the dye surface. The result is shown in Fig. 9 and shows good agreement between the model and the

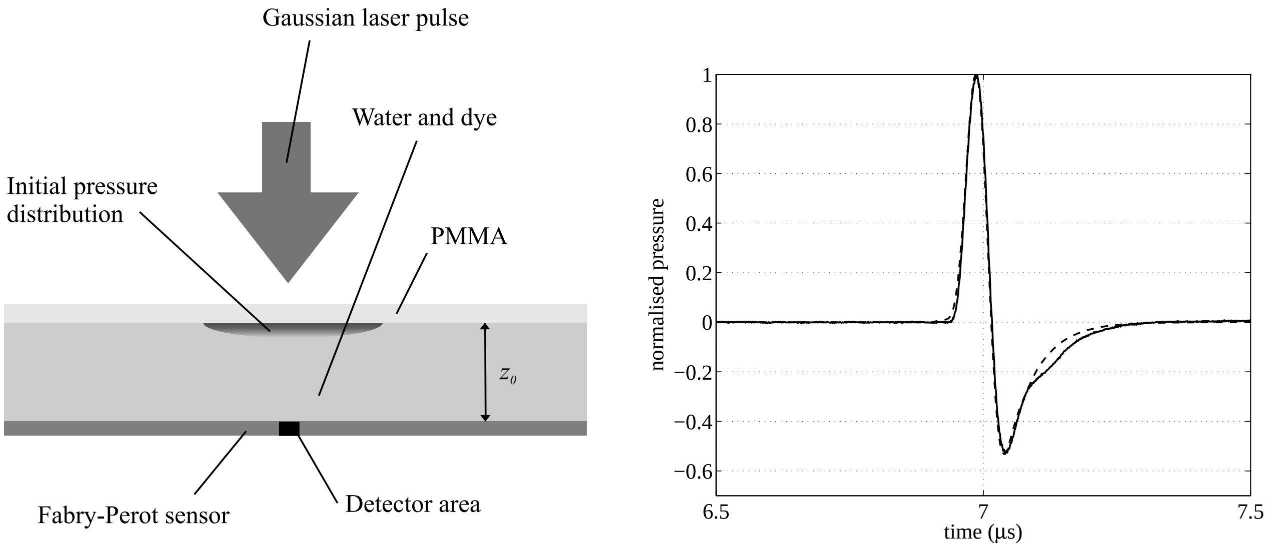

Figure 10. A Gaussian profile laser pulse, $r = 1.2$ mm at the 1/e point, was passed through a 25 mm thick transparent block of PMMA before being strongly absorbed by india ink, $\mu_a = 70$ mm^{-1}. The depth of the ink was $z_0 = 10.3$ mm. Sensor as in Fig. 9. Solid line: measurement, dashed line: model.

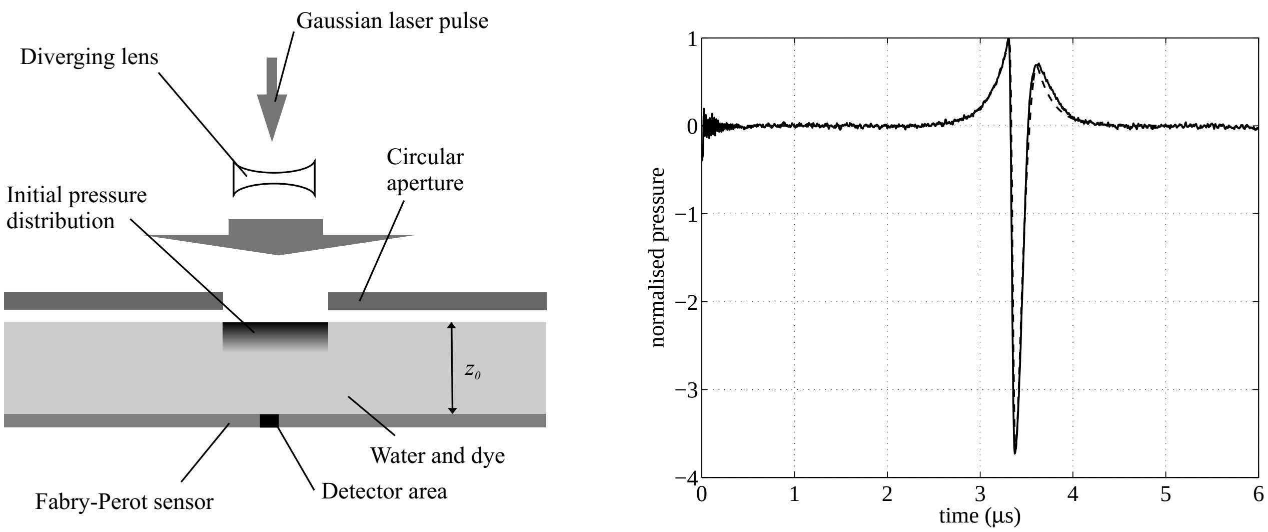

Figure 11. An expanded Gaussian profile laser pulse passes through an 1.4 mm radius aperture to give an approximation to a tophat profile. This is absorbed by a water-dye mixture, $\mu_a = 3.5$ mm^{-1}. The depth of the dye was $z_0 = 5$ mm. Sensor as in Fig. 9. Solid line: measurement, dashed line: model.

measurement. The second experiment used a similar Gaussian-shaped pulse but the light was passed through a 25 mm thick transparent block of PMMA that was in direct contact with india ink below it. The ink was strongly absorbing, $\mu_a = 70$ mm^{-1}. In this case the ink surface-to-sensor distance was $z_0 = 10.3$ mm. Fig. 10 shows the measurement and model output. There is good agreement for most of the curve but there is some discrepancy in the latter part after the negative peak. This may be due to the fact that the pulse was assumed to be perfectly circular but in practice was slightly misshapen. The Gaussian pulse was expanded through a diverging lens, in the third experiment, and a 1.4 mm radius aperture was used to give a pulse with an almost tophat profile. This tophat pulse was incident, through the PMMA, on a water-dye mixture, $\mu_a = 35$ cm^{-1}. The depth of the dye was $z_0 = 5$ mm. The slight lack of agreement in the second positive peak here may be due to the fact that the model assumed a perfect tophat profile, whereas in fact there would be some curvature in the spatial profile of the beam.

5. SUMMARY AND DISCUSSION

Two models of photoacoustic propagation in a homogeneous fluid have been described. Both calculate the response of a sensor to an arbitrary 3D initial pressure distribution. Model I calculates the whole field at any single time and can be useful for visualising the propagation. The mesh spacing need only meet the spatial Nyquist criterion and so the mesh may be many times smaller than those required for finite-element or finite-difference modelling. Arbitrarily large time steps may be used as the model uses an exact propagator and not an approximation. For large mesh sizes, i.e. high frequencies or large source-detector separations, this model becomes cumbersome. Model II, however, which calculates the field on a single plane as a function of time, speeds up the calculation of time responses considerably. Radiation patterns from photoacoustic sources may also be generated simply using this model. Preliminary pressure time series calculated using model II appear to agree well with those measured in some simple experiments.

There are several ways in which this propagation modelling may inform photoacoustic imaging. First, model II has a simple inverse which can be used as a 2D or 3D photoacoustic imaging algorithm.[18, 19] Studying the effects of the sensor response function on the predicted measured pressure, and developing an accurate model of the sensor, will inform future attempts to deconvolve the sensor point spread function from the images. Second, model II includes only the propagating part of the wavefield, ignoring the contribution made by evanescent waves. If these evanescent waves can be included into model II and then into the imaging algorithm it may be possible to achieve sub-wavelength resolution imaging over a range of a few millimetres. Lastly, model II may be useful in matched-field inversions where, typically, a forward model is used many hundreds of times. In such cases the efficiency of model II would be a boon.

ACKNOWLEDGMENTS

This work has been supported by the Engineering and Physical Sciences Research Council, UK.

REFERENCES

1. A. C. Tam, "Applications of photoacoustic sensing techniques," *Reviews of Modern Physics* **58**(2), pp. 381–431, 1986.
2. X. Wang, Y. Pang, G. Ku, X. Xie, G. Stoica, and L. V. Wang, "Noninvasive laser-induced photoacoustic tomography for structural and functional in vivo imaging of the brain," *Nature Biotechnology* **21**(7), pp. 803–806, 2003.
3. X. Wang, Y. Pang, G. Ku, G. Stoica, and L. V. Wang, "Three-dimensional laser-induced photoacoustic tomography of mouse brain with the skin and skull intact," *Optics Letters* **28**(19), pp. 1739–1741, 2003.
4. C. G. A. Hoelen, F. F. M. de Mul, R. Pongers, and A. Dekker, "Three-dimensional photoacoustic imaging of blood vessels in tissue," *Optics Letters* **23**(8), pp. 648–650, 1998.
5. P. C. Beard, "Photoacoustic imaging of blood vessel equivalent phantoms," in *Proceedings of SPIE*, **4618**, pp. 54–62, (San Jose), 2002.
6. F. Jensen, W. Kuperman, M. Porter, and H. Schmidt, *Computational Ocean Acoustics*, American Institute of Physics, New York, 1994.

7. G. Paltauf, H. Schmidt-Kloiber, and M. Frenz, "Photoacoustic waves excited in liquids by fiber-transmitted laser pulses," *Journal of the Acoustical Society of America* **104**(2), pp. 890–897, 1998.
8. L. Landau and E. Lifshitz, *Fluid Mechanics*, Butterworth Heinemann, Oxford, 2nd ed., 1987.
9. M. Tabei, T. D. Mast, and R. C. Waag, "A k-space method for coupled first-order acoustic propagation equations," *Journal of the Acoustical Society of America* **111**(1), pp. 53–63, 2002.
10. P. M. Morse and K. U. Ingard, *Theoretical Acoustics*, McGraw-Hill, 1968.
11. M. S. Howe, *Acoustics of Fluid-Structure Interactions*, CUP, 1998.
12. J. D. Jackson, *Classical Electrodynamics*, John Wiley & Sons, New York, 1962.
13. A. J. Healey, S. Leeman, and J. Weight, "Space-time imaging of transient ultrasound fields," *Int. J. Imaging Syst. Technol.* **8**, pp. 45–51, 1997.
14. P. C. Beard, F. Perennes, and T. N. Mills, "Transduction mechanisms of the fabry-perot polymer film sensing concept for wideband ultrasound detection," *IEEE Transactions on Ultrasonics Ferroelectrics and Frequency Control* **46**(6), pp. 1575–1582, 1999.
15. L. Brekhovskikh, *Waves in Layered Media*, Academic Press, New York, 1960.
16. G. Paltauf and H. Schmidt-Kloiber, "Photoacoustic cavitation in spherical and cylindrical absorbers," *Applied Physics A-Materials Science & Processing* **68**(5), pp. 525–531, 1999.
17. M. Bertero and P. Boccacci, *Introduction to Inverse Problems in Imaging*, IOP, London, 1998.
18. K. Köstli and P. Beard, "Two-dimensional photoacoustic imaging by use of fourier-transform image reconstruction and a detector with an anisotropic response," *Applied Optics* **42**(10), pp. 1899–1908, 2003.
19. K. P. Köstli, M. Frenz, H. Bebie, and H. P. Weber, "Temporal backward projection of optoacoustic pressure transients using fourier transform methods," *Physics in Medicine and Biology* **46**(7), pp. 1863–1872, 2001.